Nano Research 2014, 7(4): 544–552
DOI 10.1007/s12274-014-0422-2
Research Article

ISSN 1998-0124
CN 11-5974/O4

Study of photocurrent generation in InP nanowire-based p^+–i–n^+ photodetectors

Vishal Jain[1,2], Ali Nowzari[1], Jesper Wallentin[1], Magnus T. Borgström[1], Maria E. Messing[1], Damir Asoli[3], Mariusz Graczyk[1], Bernd Witzigmann[4], Federico Capasso[5], Lars Samuelson[1], and Håkan Pettersson[1,2] (✉)

[1] *Solid State Physics and the Nanometer Structure Consortium, Lund University, Box 118, SE-22100 Lund, Sweden*
[2] *Laboratory of Mathematics, Physics and Electrical Engineering, Halmstad University, Box 823, SE-301-18 Halmstad, Sweden*
[3] *Sol Voltaics AB, Ideon Science Park, Scheelevägen 17, SE-22370 Lund, Sweden*
[4] *Department of Computational Electronics and Photonics, University of Kassel, Wilhelmshoeher Allee 71, D-34121 Kassel, Germany*
[5] *School of Engineering and Applied Sciences, Harvard University, Cambridge, Massachusetts 02138, USA*

Received: 22 November 2013
Revised: 20 January 2014
Accepted: 21 January 2014

KEYWORDS
nanophotonics,
nanowires,
infrared (IR),
photodetectors,
solar cells

ABSTRACT

We report on electrical and optical properties of p^+–i–n^+ photodetectors/solar cells based on square millimeter arrays of InP nanowires (NWs) grown on InP substrates. The study includes a sample series where the p^+-segment length was varied between 0 and 250 nm, as well as solar cells with 9.3% efficiency with similar design. The electrical data for all devices display clear rectifying behavior with an ideality factor between 1.8 and 2.5 at 300 K. From spectrally resolved photocurrent measurements, we conclude that the photocurrent generation process depends strongly on the p^+-segment length. Without a p^+-segment, photogenerated carriers funneled from the substrate into the NWs contribute strongly to the photocurrent. Adding a p^+-segment decouples the substrate and shifts the depletion region, and collection of photogenerated carriers, to the NWs, in agreement with theoretical modeling. In optimized solar cells, clear spectral signatures of interband transitions in the zinc blende and wurtzite InP layers of the mixed-phase i-segments are observed. Complementary electroluminescence, transmission electron microscopy (TEM), as well as measurements of the dependence of the photocurrent on angle of incidence and polarization, support our interpretations.

1 Introduction

Nanowires (NWs) have attracted considerable attention due to their interesting fundamental properties and exciting prospects for applications in nanophotonics [1] e.g., light-emitting diodes (LEDs) [2], lasers [3], sensors [4] and photodetectors [5–7]. Due to the small footprint of NWs, nanophotonic III–V devices can

Address correspondence to hakan.pettersson@hh.se

be grown monolithically on silicon substrates [8–10] which is of profound importance for realizing the goals of *More than Moore: Amplifying Si technology by add-ons of other materials*. Motivated by an increasing interest in photovoltaics for conversion of solar power, there have been several reports of NW-based solar cell applications [11–13] with a 13.8% efficiency record published recently [14]. In order to optimize the design of large area photodetectors/solar cells comprising millions of NWs monolithically grown on a suitable substrate, it is crucial to understand the physical mechanisms behind the generation of photocurrent. Important related questions include e.g. the contribution of photocurrent from the substrate and influence of angle/polarization of incoming radiation on the photocurrent. To avoid complications due to formation of heterostructure barriers between NWs and substrate in such studies, a detector design with NWs and substrate made of the same material should preferably be chosen.

Here we present a detailed study of electrical and optical properties of infrared photodetectors/solar cells based on large arrays of 180 nm thick p^+–i–n^+ InP NWs vertically grown on p^+ InP substrates. In particular, we have carried out a comprehensive investigation of the mechanisms behind generation and collection of photocurrent. From analysis of photocurrent measurements on a series of samples with different p^+-segment length it is concluded that the substrate contribution to the photocurrent decreases strongly with increasing length of the p^+-segment. For p^+-segments longer than ~200 nm, the collection of photogenerated carriers funneled from the substrate into the NWs is strongly suppressed and replaced by photocurrent generated in the NWs. Moreover, the growth of extended p^+-segments leads to a compensation of residual dopants in the nominal i-segment which shifts the p–n junction further up in the NWs, strongly enhancing the absorption of light and generation of photocurrent. We also demonstrate that the electrical properties (e.g., ideality factor and dark leakage current) are generally improved by adding a p^+-segment. Finally, we discuss optical properties of newly reported record solar cells based on a similar NW design [14]. These fully optimized devices display a large photocurrent dominated by interband absorption which reveals the rich spectral signatures of the polytype crystal structure in the NWs.

2 Methods

2.1 Growth

Samples were prepared for NW growth by metal evaporation and lift-off of 30 nm Au films on a nano-imprint-defined pattern with 180 nm holes arranged in a periodic pattern of 500 nm pitch with a density of 4/μm^2 on p^+ InP (111)B substrates (Zn-doped to 5×10^{18} cm^{-3}) [15]. NWs were subsequently grown in a low-pressure (100 mbar) metal organic vapor phase epitaxy (MOVPE) system (Aixtron 200/4), with a total flow of 13 L/min using hydrogen (H_2) as carrier gas. For InP NW growth, trimethylindium (TMI) and phosphine (PH_3) were used as precursors, with constant molar fractions of $\chi^{TMI} = 35.1 \times 10^{-6}$ and $\chi^{PH_3} = 6.9 \times 10^{-3}$. Diethylzinc (DEZn) was used as p-dopant [16] and tetraethyltin (TESn) as n-dopant precursor [17]. Hydrogen chloride (HCl) at a molar fraction of $\chi^{HCl} = 4.0 \times 10^{-6}$ was used to control the radial growth [18]. The samples were first annealed at 550 °C for 10 min. under a PH_3/H_2 gas mixture to desorb any surface oxides. The reactor was then cooled to 440 °C, at which growth was initiated by adding TMI to the gas flow. After a 15 s nucleation time, HCl and DEZn were introduced and InP p^+-segments were grown with a nominal acceptor concentration of about 5×10^{18} cm^{-3} [16]. Then non-intentionally doped InP (i-segments) were grown for 8 min. Subsequently, TESn was switched on to grow InP n^+-segments for 3 min with a nominal donor concentration of about 10^{19} cm^{-3} [17, 19, 20]. Then growth was terminated and the sample cooled down in a PH_3/H_2 gas mixture. A scanning electron microscopy (SEM) image of the as-grown InP NWs is shown in Fig. 1(a). Detailed investigations by transmission electron microscopy (TEM) (Fig. S1 in the Electronic Supplementary Material (ESM)) on the present samples indicate that the p^+-segments are primarily zinc blende (ZB) whereas the intrinsic segments and n^+-segments both contain a mixture of thin wurtzite (WZ) and ZB segments, in agreement with previous reports [16, 17, 19].

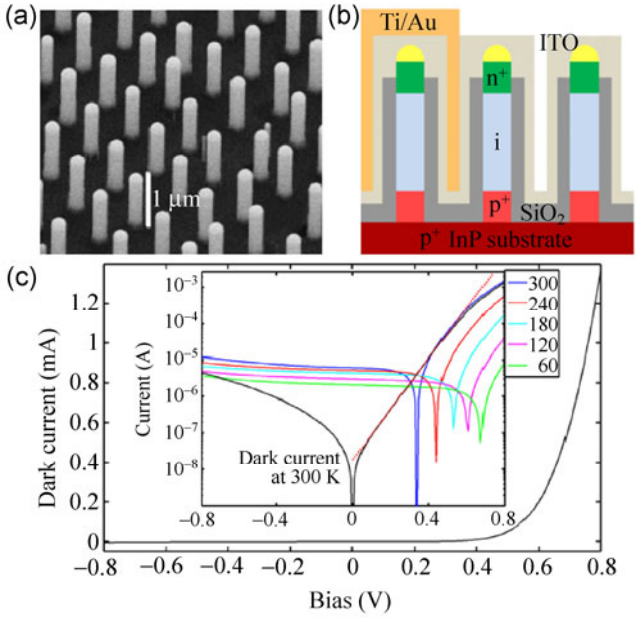

Figure 1 (a) SEM image of as-grown InP NWs. (b) Schematic detector layout. SiO_2 is used as the insulating layer and ITO as the transparent top contact. The Ti/Au contact is for bonding of the detector element. The bias is applied between the bond contact and substrate. (c) *I*–*V* characteristics of a sample with 25 nm long p^+-segments. Dark current at 300 K is shown in black color in linear scale and in semi-log scale (inset) from which an ideality factor of 2.4 is estimated (red dash-dotted trace). The inset also shows semi-log *I*–*V* plots under illumination at different temperatures.

2.2 Device fabrication

Processing of square millimeter (1 mm × 1 mm) detector elements was done by depositing insulating SiO_2 on the as-grown samples, followed by contacting the tip of the NWs using an indium tin oxide (ITO) layer (as described in Wallentin et al.) [14, 21, 22]. Figure 1(b) shows a schematic cross-section of the device layout.

2.3 Measurements

The spectrally resolved photocurrent (PC) was measured using a Bruker Vertex 80v Fourier transform spectrometer housing an integrated Janis PTSHI-950-FTIR pulse tube closed-cycle cryostat. The spectrometer was evacuated to avoid any influence of absorption lines in air. The spectrometer was equipped with a CaF_2 beam splitter and a quartz lamp. The modulated (~7.5 kHz) PC was amplified using a Keithley 428 programmable current amplifier. The current–voltage (*I*–*V*) characteristics were measured with a Keithley 6430 sub-femtoampere sourcemeter.

2.4 Modeling

For modeling of the photocurrent density in the NW detectors, a three-dimensional coupled electro-optical simulation was performed in two steps [23, 24]. The full-wave vector Helmholtz equation was first solved in the frequency domain using a finite element method approach, with a plane wave source (using the spectral shape of the tungsten lamp used in the experiments) located on top of a NW. Periodic boundary conditions were applied in-plane, creating a NW array. The refractive index was taken complex and dispersive. The local optical generation rate was calculated from this electromagnetic simulation. Photogenerated carrier and current densities were subsequently determined from the continuity equations and the Poisson equation with optical generation and spontaneous recombination rates added as local terms. The simulation is a full three-dimensional representation of the geometry, including the substrate and NWs with their respective doping profiles and material parameters (carrier mobilities, effective masses and crystal phases with respective bandgaps). The mixed-phase structure of alternating layers of ZB and WZ was treated as a 25 nm/25 nm staggered potential landscape. Thermionic emission currents connected to band-offsets were included.

3 Results and discussion

For this study we designed a series of samples with p^+–i–n^+ InP NWs grown on p^+-substrates where the nominal p^+-segment length, estimated from the growth time and SEM inspection, was varied between 0 and 250 nm, as shown in Table S1 in the ESM. In the NW samples without a p^+-segment, the corresponding lengths of the i- and n^+-segments amount to about 550 nm and 250 nm, respectively. Figure 1(a) shows an SEM image of as-grown NWs indicating a good homogeneity with respect to dimensions, shape and ordering, as expected from an imprint. Figure 1(b) shows the corresponding schematic layout of the processed detector elements.

3.1 *I*–*V* characteristics

Figure 1(c) shows typical *I*–*V* characteristics in darkness

(black traces) and under illumination (colored traces) of a sample with short (25 nm) p$^+$-segments. A clear rectifying behaviour is observed with an ideality factor of about 2.4 at 300 K. Interestingly, the ideality factor scales as ~(1/kT) as shown in Fig. S2 in the ESM. We observed the same behaviour in previously reported I–V data for i-n$^+$ NWs grown directly on p$^+$-substrates [21]. It is interesting to note that similar temperature-dependent ideality factors were previously reported for disordered organic p–n junctions [25]. The deviation from classical transport models was attributed to violation of the Einstein relation $\left(\frac{qD}{\mu} = kT\right)$ in the framework of diffusion theory. In view of the polytype structure of the NWs studied in the present work, similar arguments could explain our results. From Fig. 1(c) it is also evident that the open-circuit voltage, V_{OC}, decreases with increasing temperature as expected. For an ideal diode or solar cell, $V_{OC}(T) = \frac{kT}{q}\ln\left(\frac{I_{SC}}{I_o}\right)$, where I_{SC} is the short-circuit current and I_o the saturation (reverse leakage) current. The temperature dependence of V_{OC} stems primarily from the strong temperature dependence of the saturation current $I_o \sim n_i^2$, where n_i is the intrinsic carrier concentration. Extrapolating V_{OC} to low temperatures gives an approximate value of the corresponding bandgap. In our case, we observe a value of about 0.7 V for samples with short (25 nm) p$^+$-segments which increases to about 1.1 V for samples with long (200 nm) p$^+$-segments. The main reason for a larger extrapolated value for samples with long p$^+$-segments is the reduced junction area, and thus reduced dark current, compared to samples without p$^+$-segments. A contributing factor to the reduced extrapolated value compared to the InP bandgap, even for the longest p$^+$-segment samples, could be a voltage drop over the Schottky-like contact formed at the Au

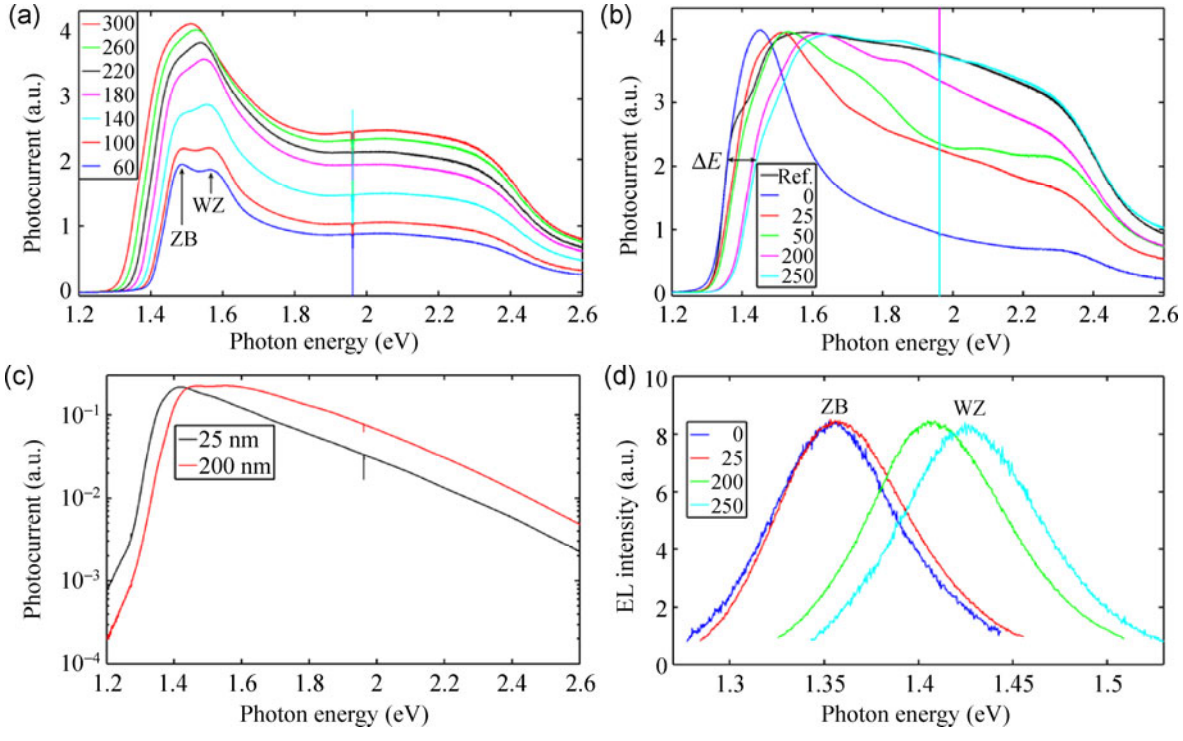

Figure 2 (a) Spectrally resolved short-circuit photocurrent of a sample with 25 nm p$^+$-segments measured at different temperatures (60–300 K). The photocurrent has been normalized with respect to the photon flux of the tungsten lamp using a Si photodiode. The sharp signal at 1.96 eV is due to the built-in red laser used in the Fourier transform spectrometer to keep track of the position of the scanning mirror. (b) Spectrally resolved short-circuit photocurrent of samples with varying p$^+$-segment length (0–250 nm) measured at 300 K, along with a planar reference mesa InP sample (Ref.). The photocurrent has been normalized for comparison. (c) Semi-log plot of the spectrally resolved photocurrent for samples with 25 nm and 200 nm p$^+$-segments, at 300 K. (d) Electroluminescence from the same samples as in (b) at 300 K.

catalyst/NW interface. Such a voltage drop has been recently discussed for Au/GaAs NWs [26, 27]. The general trends observed upon increasing the p^+-segment length e.g. increase in V_{OC}, improvement in ideality factor and decrease in reverse dark current level (see Fig. S3 in the ESM) reflect a deviation from ideal diode conditions when the substrate actively becomes part of a NW p^+–i–n^+ device.

3.2 Photocurrent and electroluminescence measurements

Figure 2(a) shows temperature-dependent spectrally resolved short-circuit photocurrent spectra for a sample with 25 nm p^+-segments (discussed above). All spectra were normalized with respect to the photon flux using a calibrated Si photodiode. The peak marked with "ZB" in the spectra agrees well with the fundamental interband transition energy of bulk InP, which we interpret in terms of photoexcitation of the p^+ substrate and subsequent funneling of the photogenerated minority carriers into the NWs. A small contribution from the thin ZB layers in the mixed-phase (predominantly WZ) i-region of the NWs probably also contributes to the photocurrent signal. As discussed below, diffusion plays an important role in the funneling process, since the penetration of the space charge region at the foot of the NWs into the substrate is merely a few tens of nm given the high substrate doping concentration (5×10^{18} cm^{-3}). This conclusion is in agreement with previously reported photocurrent spectra for NW-based photodetectors without a p^+-segment [21]. The bandgap of pure WZ InP is known to be at least 80 meV larger than for ZB InP [28–31]. The peak marked by "WZ" indicates a contribution to the photocurrent from interband transitions in the thin WZ layers of the mixed-phase i-segments of the NWs.

A striking difference observed by comparing the spectrally resolved photocurrent collected for samples with different p^+-segment lengths is the gradual shift, ΔE, in onset energy of the photocurrent, as shown in Figs. 2(b) and 2(c) (in semi-log scale). We interpret this shift in terms of a less efficient collection of photogenerated carriers from the substrate as the p^+-segment effectively decouples the substrate from the active NW p^+–i–n^+ junctions. Moving the junction up into the NW leads to a redistribution of the electric field in the NW/substrate. As the length of the p^+-segments becomes comparable to the minority carrier diffusion length (~160 nm) [16], funneling of photogenerated minority carriers from the substrate is lost and replaced by collection of carriers from the i-segment of the NWs providing a dominant WZ signal. Electroluminescence (EL) measurements on the same samples (Fig. 2(d)) confirm our interpretation of the photocurrent data, since samples with short p^+-segments display mainly ZB luminescence, whereas mainly contributions from WZ is observed from samples with long p^+-segments.

3.3 Modeling

A decreased substrate contribution to the photocurrent for samples with extended p^+-segments is furthermore expected from sophisticated modeling of the devices. Figure 3 shows plots of calculated electron current densities at short-circuit conditions for NW samples without (Fig. 3(a)) and with 250 nm p^+-segment in the NWs (Fig. 3(b)). Evidently, there is a significant substrate contribution to the photocurrent for samples without a p^+-segment. The physical mechanism behind this photocurrent is diffusion-driven funneling of photogenerated carriers from the substrate into the NWs. The carriers, driven by the concentration gradient from substrate to the substrate/NW interface, are subsequently collected by the electric field in the NWs. The white iso-line represents the separator between downward parasitic (towards the p^+-contact) and upward (towards the n^+-contact) electron flows (current densities in opposite directions). In the absence of any p^+-segment (Fig. 3(a)), the active region from which photogenerated carriers are funneled into the NWs extends > 200 nm into the substrate. In contrast, the substrate is more or less decoupled from the active NWs with 250 nm p^+-segments (Fig. 3(b)), resulting in a vanishing electron current density contribution from the substrate.

3.4 Discussion of p^+-segment series samples

Another pronounced difference observed by comparing the spectrally resolved photocurrents displayed in Fig. 2 is the strong decrease in signal above about

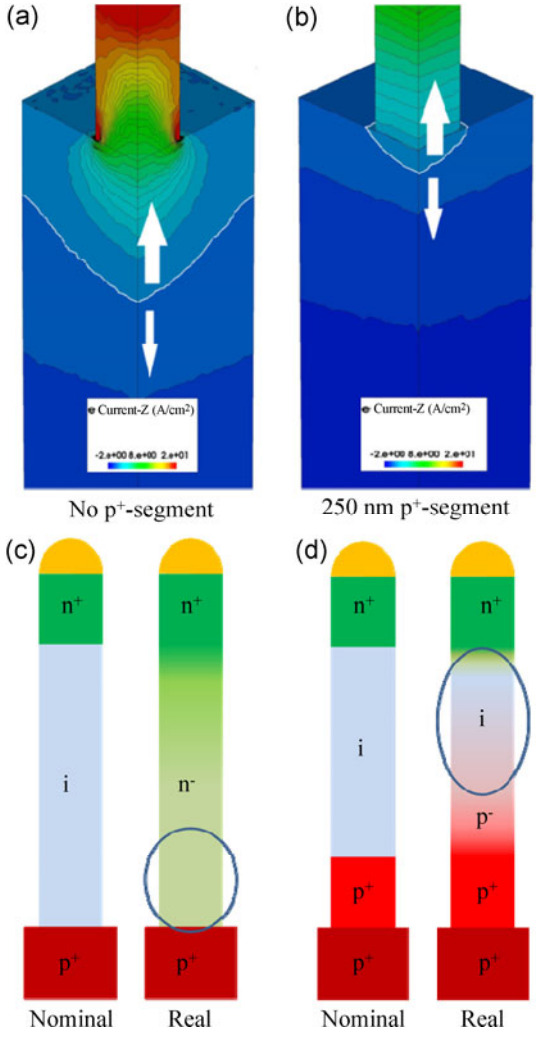

Figure 3 Color-coded plot of calculated photogenerated electron current density for a NW detector (a) without a p^+-segment and (b) with a 250 nm p^+-segment in the NW. The arrows indicate the direction of the electron flow, upward leading to extracted photocurrent and downward to a small parasitic current. Schematic comparisons of the plausible real doping profiles as compared to nominal doping profiles in NWs (c) without a p^+-segment and (d) with a 250 nm p^+-segment. The effect of residual n-doping is shown in (c). In (d) the residual n-doping is compensated by a Zn (acceptor) reservoir effect due to the growth of an extended p^+-segment. The blue ovals show the varying position of the p–n junction along the NWs.

1.6 eV for samples with shorter p^+-segments. In this part of the spectrum, most of the light is absorbed near the top of the NWs due to resonant absorption [32], wherefore it is crucial to minimize the length of the n^+-segment to efficiently collect these carriers [14]. One explanation for the relatively poor efficiency observed for our devices without a p^+-segment is that the nominally undoped i-segment is in fact most likely weakly n-type, as is normally the case for InP [19]. A residual n-doping concentration of 10^{16} cm^{-3} would result in a (high-field) depletion region localized in the lower part of the NWs (see Fig. 3(c)). The remaining part of the weakly n-type NW (including the top n^+-segment) amounts to about 400 nm. This region is characterized by a low electric field and thus poor collection efficiency. A significant photocurrent contribution in this case therefore stems from collection of photogenerated carriers from the substrate as discussed above. With increasing p^+-segment length the junction formed at the interface between the p^+-segment and i-segment, and thus the depletion region, is shifted upwards in the NWs. Furthermore, a Zn doping reservoir effect, similar to the one discussed in Amit et al. [33], would compensate the background n-doping in the i-segment and move the p–n junction further up in the NW as shown in Fig. 3(d). With the electric field region (p–n junction) reaching near the top of the NWs, better matching the absorption profile in the NWs as discussed above [14, 32], the collection efficiency is strongly improved which results in a larger photocurrent in the high energy part of the spectrum. A further possible mechanism that enhances the photocurrent generation for longer p^+-segments has to do with the growth rate of the NWs. We observe that as the p^+-segment length is increased the effective NW growth rate decreases, indicating that the i-/n^+-segment lengths are slightly reduced which enhances the collection of photogenerated carriers as discussed above. The reduced growth rate can be explained in terms of a reduced surface diffusion on the Zn doped p^+-segments, which in turn reduces the amount of growth material reaching the seed particle [34]. For comparison, a spectrally resolved photocurrent spectrum (black trace) of a planar InP ZB p^+–i–n^+ mesa sample is also shown in Fig. 2(b). The thicknesses of the i-layer and top n^+-layer are about 1 μm and 200 nm, respectively. Although not identical, it is evident that the overall shape of the photocurrent at higher photon energy for the NW detectors successively becomes more similar to the planar detector as the length of the p^+-segments in the NWs is increased. From this plot it is also evident that the effective top n-region of the NWs with shorter p^+-segments, indeed

must be considerably longer than 200 nm.

3.5 Discussion of solar cell samples

For comparison, we have also performed a detailed study of solar cells with 9.3% efficiency from the same series as the reported 13.8% record samples [14]. The design is similar to the one used for the varying p^+-segment series, except for slightly longer p^+-segments (350 nm), considerably longer i-segments (1 μm) and shorter n^+-segments (180 nm). In addition, the catalytic Au particles were removed before fabricating the top ITO contact. The latter process step improves the electrical properties by eliminating any possible Schottky barrier present between the Au catalyst particles and NWs [26]. A clear improvement of the *I*–*V* characteristics compared to the previously described series of samples with varying p^+-segment length is indeed observed, as shown in Fig. S4 in the ESM. The extrapolated open-circuit voltage has increased compared to the p^+-segment series. It is also noted that V_{OC} actually saturates at a temperature below 40 K. This behavior signals significant deviations from ideal solar cell characteristics, which might be related to e.g. a temperature dependent ideality factor (discussed above). Removal of the Au catalyst particles is also expected to enhance the photocurrent, since they have been shown to scatter incoming radiation leading to significant losses [32]. In comparison to the sample series discussed above, the modified design parameters for the solar cells favor a dominant generation and collection of carriers in the mixed-phase i-segments of the NWs [35] as evidenced by the spectrally resolved photocurrent data shown in Fig. 4. The 60 K spectrum shows spectral signatures which we interpret in terms of optical excitations involving the crystal field-split valence bands of WZ InP (A and B peaks separated by 30 meV) and the spin-split valence band (C peak separated by 160 meV from the A-peak) [36, 37]. We also note that there is a small photocurrent contribution from the corresponding ZB layers in the i-segments. The inset of Fig. 4 shows the accumulated (all wavelength) photocurrent from the same sample for different angle of incidence θ of incoming radiation, together with a $\cos(\theta)$ fitting. The overall agreement between experimental data and fitting supports the idea of NW-based solar cells behaving similar to planar devices regarding incident angle dependence. The good agreement is somewhat unexpected given the relatively complex composition and geometry of the present devices, including e.g. different absorption coefficients for light impinging perpendicular and parallel to a NW axis. However, the inset reveals a slightly reduced photocurrent at large angle compared to the fitting. A similar effect, typically observed also for planar p–i–n solar cells, is attributed to an enhanced reflection at large angles [38]. Figure S5 in the ESM shows the spectrally resolved photocurrent for different polarization of incoming radiation with normal (0°) and 45° incidence. As expected, the photocurrent shows no polarization dependence for normal incidence, since the electric field is perpendicular to the NW axis for both polarization directions. For tilted conditions, there is a slightly larger relative photocurrent contribution, compared to normal incidence, at higher photon energy, which probably reflects a decreased absorption in the top n-segment as previously discussed. For tilted conditions, there is also a slightly larger relative contribution at higher photon energy in the case of parallel polarization, compared to perpendicular polarization, probably due to slightly larger absorption coefficients when the electric field is parallel to the NW.

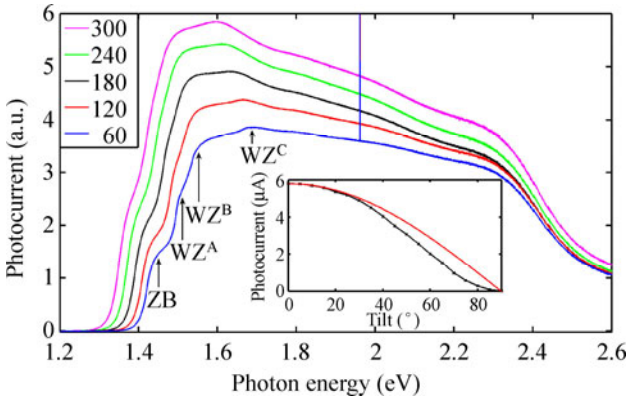

Figure 4 Spectrally resolved short-circuit photocurrent of a 9.3% efficiency solar cell sample, measured at different temperatures, exhibiting interband transitions in the ZB and WZ layers in the mixed-phase i-region of the NWs. The bottom inset shows the angular dependence of the integrated short-circuit photocurrent (I_{SC}) at 300 K (black trace). The red trace shows a $k \cdot \cos(\theta)$ fitting to the experimental data with a constant k.

4 Conclusions

We have presented electrical and optical data for near-infrared p^+–i–n^+ photodetectors/solar cells based on large arrays of InP NWs grown on InP substrates. From spectrally resolved measurements, we conclude that the photocurrent collection process depends strongly on the p^+-segment length. Without p^+-segments, the photocurrent is dominated by funneling photo-generated carriers from the substrate into the NWs. Adding a p^+-segment in the NWs favors collection of carriers generated in the i-region of the NWs since the junction is moved up into the NWs which decouples the substrate from the active device and leads to a more well-defined electric field distribution in the i-segments, all in agreement with theoretical modeling. In solar cell samples, clear signatures of interband transitions in the ZB and WZ InP layers of the mixed-phase i-region are observed. Complementary measurements of the dependence of the photocurrent on angle of incidence and polarization of the incoming radiation support our interpretations.

Acknowledgements

The authors acknowledge financial support from the Nanometer Structure Consortium nmC@LU, Halmstad University, the Erik Johan Ljungberg Foundation, the Carl Trygger Foundation, the Swedish Research Council, the Swedish National Board for Industrial and Technological Development, the Swedish Foundation for Strategic Research, the Swedish Energy Agency and the EU program AMON-RA (No. 214814).

Electronic Supplementary Material: Supplementary material (p^+-segment lengths for different samples, TEM image of a single p^+–i–n^+ InP NW, temperature dependent *I*–*V* data for different samples, polarization- and incident angle dependence of spectrally resolved photocurrent for a 9.3% efficiency solar cell) is available in the online version of this article at http://dx.doi.org/10.1007/s12274-014-0422-2.

References

[1] Yan, R. X.; Gargas, D.; Yang, P. D. Nanowire photonics. *Nat. Photonics* **2009**, *3*, 569–576.

[2] Duan, X. F.; Huang, Y.; Cui, Y.; Wang, J. F.; Lieber, C. M. Indium phosphide nanowires as building blocks for nanoscale electronic and optoelectronic devices. *Nature* **2001**, *409*, 66–69.

[3] Huang, M. H.; Mao, S.; Feick, H.; Yan, H. Q.; Wu, Y. Y.; Kind, H.; Weber, E.; Russo, R.; Yang, P. D. Room-temperature ultraviolet nanowire nanolasers. *Science* **2001**, *292*, 1897–1899.

[4] Patolsky, F.; Lieber, C. M. Nanowire nanosensors. *Mat. Today* **2005**, *8*, 20–28.

[5] Soci, C.; Zhang, A.; Bao, X. Y.; Kim, H.; Lo, Y.; Wang, D. Nanowire photodetectors. *J. Nanosci. Nanotechnol.* **2010**, *10*, 1430–1449.

[6] Wang, J. F.; Gudiksen, M. S.; Duan, X. F.; Cui, Y.; Lieber, C. M. Highly polarized photoluminescence and photodetection from single indium phosphide nanowires. *Science* **2001**, *293*, 1455–1457.

[7] Pettersson, H.; Trägårdh, J.; Persson, A. I.; Landin, L.; Hessman, D.; Samuelson, L. Infrared photodetectors in heterostructure nanowires. *Nano Lett.* **2006**, *6*, 229–232.

[8] Mårtensson, T.; Svensson, C. P. T.; Wacaser, B. A.; Larsson, M. W.; Seifert, W.; Deppert, K.; Gustafsson, A.; Wallenberg, L. R.; Samuelson, L. Epitaxial III−V nanowires on silicon. *Nano Lett.* **2004**, *4*, 1987–1990.

[9] Svensson, C. P. T.; Mårtensson, T.; Trägårdh, J.; Larsson, C.; Rask, M.; Hessman, D.; Samuelson, L.; Ohlsson, J. Monolithic GaAs/InGaP nanowire light emitting diodes on silicon. *Nanotechnology* **2008**, *19*, 305201.

[10] Wei, W.; Bao, X. Y.; Soci, C.; Ding, Y.; Wang, Z. L.; Wang, D. L. Direct heteroepitaxy of vertical InAs nanowires on Si substrates for broad band photovoltaics and photodetection. *Nano Lett.* **2009**, *9*, 2926–2934.

[11] LaPierre, R. R. Theoretical conversion efficiency of a two-junction III–V nanowire on Si solar cell. *J. Appl. Phys.* **2011**, *110*, 04310.

[12] Tian, B. Z.; Zheng, X. L.; Kempa, T. J.; Fang, Y.; Yu, N. F.; Yu, G. H.; Huang, J. L.; Lieber, C. M. Coaxial silicon nanowires as solar cells and nanoelectronic power sources. *Nature* **2007**, *449*, 885–889.

[13] Giacomo, M.; Scofield, A. C.; Hung, C. H.; Huffaker, D. L. GaAs nanopillar-array solar cells employing *in situ* surface passivation. *Nat. Commun.* **2013**, *4*, 1497.

[14] Wallentin, J.; Anttu, N.; Asoli, D.; Huffman, M.; Åberg, I.; Magnusson, M. H.; Siefer, G.; Fuss-Kailuweit, P.; Dimroth, F.; Witzigmann, B. et al. InP nanowire array solar cells achieving 13.8% efficiency by exceeding the ray optics limit. *Science* **2013**, *339*, 1057–1060.

[15] Mårtensson, T.; Carlberg, P.; Borgström, M.; Montelius, L.; Seifert, W.; Samuelson, L. Nanowire arrays defined by nanoimprint lithography. *Nano Lett.* **2004**, *4*, 699–702.

[16] Wallentin, J.; Wickert, P.; Ek, M.; Gustafsson, A.; Wallenberg, L. R.; Magnusson, M. H.; Samuelson, L.; Deppert, K.; Borgström, M. T. Degenerate p-doping of InP nanowires for large area tunnel diodes. *Appl. Phys. Lett.* **2011**, *99*, 253105.

[17] Borgström, M. T.; Norberg, E.; Wickert, P.; Nilsson, H. A.; Trägårdh, J.; Dick, K. A.; Statkute, G.; Ramvall, P.; Deppert, K.; Samuelson, L. Precursor evaluation for *in situ* InP nanowire doping. *Nanotechnology* **2008**, *19*, 445602.

[18] Borgström, M. T.; Wallentin, J.; Trägårdh, J.; Ramvall, P.; Ek, M.; Wallenberg, L. R.; Samuelson, L.; Deppert, K. *In-situ* etching for total control over axial and radial nanowire growth. *Nano Res.* **2010**, *3*, 264–270.

[19] Wallentin, J.; Ek, M.; Wallenberg, L. R.; Samuelson, L.; Borgström, M. T. Electron trapping in InP nanowire FETs with stacking faults. *Nano Lett.* **2012**, *12*, 151–155.

[20] Minot, E. D.; Kelkensberg, F.; Kouwen, M. V.; Dam, J. A. V.; Kouwenhoven, L. P.; Zwiller, V.; Borgström, M. T.; Wunnicke, O.; Verheijen, M. A.; Bakkers, E. P. A. M. Single quantum dot nanowire LEDs. *Nano Lett.* **2007**, *7*, 367–371.

[21] Pettersson, H.; Zubritskaya, I.; Nghia, N. T.; Wallentin, J.; Borgström, M. T.; Storm, K.; Landin, L.; Wickert, P.; Capasso, F.; Samuelson, L. Electrical and optical properties of InP nanowire ensemble p^+–i–n^+ photodetectors. *Nanotechnology* **2012**, *23*, 135201.

[22] Borgström, M. T.; Wallentin, J.; Heurlin, M.; Fält, S.; Wickert, P.; Leene, J.; Magnusson, M. H.; Deppert, K.; Samuelson, L. Nanowires with promise for photovoltaics. *IEEE J. Sel. Top. Quantum Electron.* **2011**, *17*, 1050–1061.

[23] Yu, S.; Kupec, J.; Witzigmann, B. Efficiency analysis of III–V axial and core–shell nanowire solar cells. *J. Comput. Theo. Nano.* **2012**, *9*, 688–695.

[24] Kupec, J.; Witzigmann, B. Computational electromagnetics for nanowire solar cells. *J. Comput. El.* **2012**, *11*, 153–165.

[25] Harada, K.; Werner, A. G.; Pfeiffer, M.; Bloom, C. J.; Elliott, C. M.; Leo, K. Organic homojunction diodes with a high built-in potential: Interpretation of the current–voltage characteristics by a generalized Einstein relation. *Phys. Rev. Lett.* **2005**, *94*, 036601.

[26] Han, N.; Wang, F. Y.; Yip, S.; Hou, J. J.; Xiu, F.; Shi, X. L.; Hui, A. T.; Hung, T.; Ho, J. C. GaAs nanowire Schottky barrier photovoltaics utilizing Au–Ga alloy catalytic tips. *Appl. Phys. Lett.* **2012**, *101*, 013105.

[27] Suyatin, D. B.; Jain, V.; Nebol'sin, V. A.; Trägårdh, J.; Messing, M. E.; Wagner, J. B.; Persson, O.; Timm, R.; Mikkelsen, A.; Maximov, I. et al. Strong Schottky barrier reduction at Au-catalyst/GaAs-nanowire interfaces by electric dipole formation and Fermi-level unpinning. *Nat. Commun.* **2014**, *5*, 3221.

[28] Mattila, M.; Hakkarainen, T.; Mulot, M.; Lipsanen, H. Crystal-structure-dependent photoluminescence from InP nanowires. *Nanotechnology* **2006**, *17*, 1580.

[29] Mishra, A.; Titova, L. V.; Hoang, T. B.; Jackson, H. E.; Smith, L. M.; Yarrison-Rice, J. M.; Kim, Y.; Joyce, H. J.; Gao, Q.; Tan, H. H. et al. Polarization and temperature dependence of photoluminescence from zincblende and wurtzite InP nanowires. *Appl. Phys. Lett.* **2007**, *91*, 263104.

[30] Pemasiri, K.; Montazeri, M.; Gass, R.; Smith, L. M.; Jackson, H. E.; Yarrison-Rice, J.; Paiman, S.; Gao, Q.; Tan, H. H.; Jagadish, C. et al. Carrier dynamics and quantum confinement in type Ⅱ ZB–WZ InP nanowire homostructures. *Nano Lett.* **2009**, *9*, 648–654.

[31] Bao, J. M.; Bell, D. C.; Capasso, F.; Wagner, J. B.; Mårtensson, T.; Trägårdh, J.; Samuelson, L. Optical properties of rotationally twinned InP nanowire heterostructures. *Nano Lett.* **2008**, *8*, 836–841.

[32] Anttu, N.; Xu, H. Q. Coupling of light into nanowire arrays and subsequent absorption. *J. Nanosci. Nanotechnol.* **2010**, *10*, 7183–7187.

[33] Amit, I.; Givan, U.; Connell, J. G.; Paul, D. F.; Hammond, J. S.; Lauhon, L. J.; Rosenwaks, Y. Spatially resolved correlation of active and total doping concentrations in VLS grown nanowires. *Nano Lett.* **2013**, *13*, 2598–2604.

[34] Wallentin, J.; Messing, M. E.; Trygg, E.; Samuelson, L.; Deppert, K.; Borgström, M. T. Growth of doped $InAs_yP_{1-y}$ nanowires with InP shells. *J. Cryst. Growth* **2011**, *331*, 8–14.

[35] Anttu, N.; Xu, H. Q. Efficient light management in vertical nanowire arrays for photovoltaics. *Opt. Express* **2013**, *21*, A558–A575.

[36] Perera, S.; Pemasin, K.; Fickenscher, M. A.; Jackson, H. E.; Smith, L. M.; Yarrison-Rice, J.; Paiman, S.; Gao, Q.; Tan, H. H.; Jagadish, C. Probing valence band structure in wurtzite InP nanowires using excitation spectroscopy. *Appl. Phys. Lett.* **2010**, *97*, 023106.

[37] Tuin, G. L.; Borgström, M. T.; Trägårdh, J.; Ek, M.; Wallenberg, L. R.; Samuelson, L.; Pistol, M. E. Valence band splitting in wurtzite InP nanowires observed by photoluminescence and photoluminescence excitation spectroscopy *Nano Res.* **2011**, *4*, 159–163.

[38] Heinämäki, A.; Guekos, G. Solar cell short-circuit current dependence on the angle of the incident radiation. *Sol. Cells* **1987**, *20*, 65–73.